



Article

Synergistic Use of the SRAL/MWR and SLSTR Sensors on Board Sentinel-3 for the Wet Tropospheric Correction Retrieval

Pedro Aguiar ^{1,2,*} , Telmo Vieira ^{1,2} , Clara Lázaro ^{1,2} and M. Joana Fernandes ^{1,2}

¹ Departamento de Geociências, Ambiente e Ordenamento do Território, Faculdade de Ciências, Universidade do Porto, rua do Campo Alegre s/n, 4169-007 Porto, Portugal; telmo.vieira@fc.up.pt (T.V.); clazaro@fc.up.pt (C.L.); mjfernan@fc.up.pt (M.J.F.)

² Centro Interdisciplinar de Investigação Marinha e Ambiental (CIIMAR), Terminal de Cruzeiros de Leixões, Av. General Norton de Matos s/n, 4450-208 Matosinhos, Portugal

* Correspondence: pedro.aguiar@fc.up.pt

Abstract: The Sentinel-3 satellites are equipped with dual-band Microwave Radiometers (MWR) to derive the wet tropospheric correction (WTC) for satellite altimetry. The deployed MWR lack the 18 GHz channel, which mainly provides information on the surface emissivity. Currently, this information is considered using additional parameters, one of which is the sea surface temperature (SST) extracted from static seasonal tables. Recent studies show that the use of a dynamic SST extracted from Numerical Weather Models (ERA5) improves the WTC retrieval. Given that Sentinel-3 carries on board the Sea and Land Surface Temperature Radiometer (SLSTR), from which SST observations are derived simultaneously with those of the Synthetic Aperture Radar Altimeter and MWR sensors, this study aims to develop a synergistic approach between these sensors for the WTC retrieval over open ocean. Firstly, the SLSTR-derived SSTs are evaluated against the ERA5 model; secondly, their impact on the WTC retrieval is assessed. The results show that using the SST input from SLSTR, instead of ERA5, has no impact on the WTC retrieval, both globally and regionally. Thus, for the WTC retrieval, there seems to be no advantage in having collocated SST and radiometer observations. Additionally, this study reinforces the fact that the use of dynamic SST leads to a significant improvement over the current Sentinel-3 WTC operational algorithms.

Keywords: satellite altimetry; wet tropospheric correction; Sentinel-3



Citation: Aguiar, P.; Vieira, T.; Lázaro, C.; Fernandes, M.J. Synergistic Use of the SRAL/MWR and SLSTR Sensors on Board Sentinel-3 for the Wet Tropospheric Correction Retrieval. *Remote Sens.* **2022**, *14*, 3231. <https://doi.org/10.3390/rs14133231>

Academic Editor: Zhenzhan Wang

Received: 13 May 2022

Accepted: 30 June 2022

Published: 5 July 2022

Publisher's Note: MDPI stays neutral with regard to jurisdictional claims in published maps and institutional affiliations.



Copyright: © 2022 by the authors. Licensee MDPI, Basel, Switzerland. This article is an open access article distributed under the terms and conditions of the Creative Commons Attribution (CC BY) license (<https://creativecommons.org/licenses/by/4.0/>).

1. Introduction

The satellite radar altimetry sea surface height (SSH) is a key observation derived from this remote sensing technique, which can be obtained with centimetric accuracy over open ocean [1]. The long-term analysis of SSH measurements is crucial for, e.g., climate change-related sea level variation studies [2]. For the precise SSH estimation, a series of corrections need to be applied to the range measured by the altimeter, namely corrections related to instrumental effects, range, and geophysical corrections. In the computation of the altimeter range, the emitted electromagnetic pulse is assumed to travel at the speed of light, c . However, when travelling through the atmosphere, its velocity is inferior to c , thus leading to an overestimation of the altimeter range and a subsequent underestimation of the SSH. Thus, in the computation of the corrected SSH, all the range corrections are negative values that are added to the SSH initially obtained.

Amongst the range corrections, one of the most significant error sources is the one due to the path delay in the altimeter signal induced by the wet component of the troposphere [3]. This path delay is mostly due to the interaction of the altimeter emitted pulse with the tropospheric water vapour. The corresponding correction, the wet tropospheric correction (WTC), can reach, in absolute terms, almost 50 centimetres for the highest concentrations of atmospheric water vapour, with a standard deviation that can

reach 15 centimetres [3]. Any error in the computation of this range correction can lead to a misinterpretation of SSH variations.

Due to its large spatial and temporal variability, the most accurate way to determine the WTC is through the measurements of nadir-viewing microwave radiometers (MWR) on board the altimetric missions, collocated with the altimeter observations. With this purpose in mind, since the launch of ERS-1 by the European Space Agency (ESA) in 1991, and TOPEX/Poseidon (TP) by NASA/CNES in 1992, the main altimetric satellites have been equipped with an on board MWR.

Two types of MWR instruments are used on board altimetry missions, with two or three frequency bands. The three-band MWR are deployed on the reference missions, namely on TP, Jason-1, Jason-2, Jason-3, and the most recent Sentinel-6 Michael Freilich, whereas the dual-band MWR operate on board ESA's satellites, such as ERS-1, ERS-2, Envisat and the Sentinel-3 mission, on the Geosat Follow-On (GFO) and on the ISRO/CNES SARAL/ALtiKa mission.

The main frequency band for both instruments is in the 21–23.8 GHz atmospheric window, very close to the water absorption band peaked at the 22.235 GHz, making it particularly sensitive to the atmospheric water vapour content. The second frequency band common to both MWR instruments is located in the 34–37 GHz window, specifically sensitive to the atmospheric cloud liquid water content. The third frequency, located in the 18–18.7 GHz atmospheric window, is deployed only on the reference missions MWR, allowing the consideration of sea surface wind effects in ocean emissivity and the corresponding signature on the MWR brightness temperatures (TB) measurements [3].

The inverse function used to retrieve the WTC from the MWR brightness temperatures is usually empirically established using statistical regression algorithms, namely log-linear algorithms in the case of the reference missions [4,5], and neural networks for the ESA's missions [6–8]. For retrieval purposes, it has been shown that the three-band MWR are best suited for the measurement of the WTC [4,9]. In the case of the ESA's missions, in which dual-band MWR are deployed, the retrieval of the WTC is done considering additional parameters, to compensate for the lack of the 18–18.7 GHz band.

For the Sentinel-3 mission, two types of WTC products are provided, retrieved from neural network algorithms with three or five inputs [6,7]. Both networks' architectures were first developed for the Envisat mission, consisting of one hidden layer with eight neurons and a linear output layer. The input parameters for the first neural network algorithm are the MWR brightness temperatures, measured at 23.8 GHz and 36.5 GHz, and the ocean backscatter coefficient σ_0 at Ku-band (not corrected for the atmospheric attenuation). The five-inputs neural network, expected to be an improvement on the first, considers the same three parameters together with the sea surface temperature (SST), extracted from four static seasonal tables, and the atmospheric temperature vertical decrease rate between the surface and the 800 hPa pressure level, γ_{800} , extracted from a static climatological table.

Although both neural network algorithms are used operationally for the Sentinel-3 mission, recent studies indicate that they are not optimized for this mission [8,10]. Additionally, the study carried out by [8] suggests that the inclusion of the SST as a dynamic input allows a better mapping of the surface contribution in the WTC retrieval, whereas the γ_{800} parameter provides redundant information.

While the two TB measurements from the Sentinel-3 MWR are collocated with the radar altimeter σ_0 parameter, this is not the case for the SST parameter. As proposed by [8], the last can be extracted from the European Centre for Medium-Range Weather Forecasts (ECMWF) atmospheric models' grids, requiring a spatial and temporal interpolation for each along-track altimeter measurement position.

Besides the dual frequency (Ku and C band) Synthetic Aperture Radar Altimeter (SRAL) and the dual frequency passive MWR, the Global Monitoring for Environment and Security (GMES) Sentinel-3 mission from the Copernicus program disposes of the Sea and Land Surface Temperature Radiometer (SLSTR), which provides, among other observations, SST_{skin} gridded measurements over the ocean collocated with those from the

SRAL/MWR sensors [11]. The SST_{skin} is defined as the ocean temperature within the water layer with a maximum depth of $\sim 10 \mu m$.

In this context, the objective of this study is the assessment of the SLSTR-derived SST_{skin} measurements as an input for the retrieval of the WTC of Sentinel-3 SRAL observations over open ocean. The motivation for this study is to take advantage of the collocation between the SRAL/MWR and SLSTR sensors measurements that do not require spatial and temporal interpolations as is the case with the SST derived from ECMWF models, as proposed by [8].

This paper is organized as follows: Section 2 describes the data and methodology used; in Section 3, the results and discussion are presented; the final section, Section 4, is reserved for the conclusions of the work.

2. Data and Methods

This work comprises three main tasks: (1) synergistic use of the Sentinel-3A SLSTR and SRAL/MWR sensors data, to derive the SST_{skin} from the first sensor to the geographical position of each SRAL along-track observation; (2) evaluation of the SLSTR-derived SST_{skin} against the SST_{skin} interpolated from the ECMWF ERA5 atmospheric model, at each SRAL/MWR data observation; and (3) assessment of the impact of using the SST_{skin} derived from each retrieval source (SLSTR sensor and ERA5 atmospheric model), alongside the two MWR brightness temperatures, the altimeter backscatter coefficient, σ_0 , and the atmospheric temperature lapse rate, γ_{800} , for the retrieval of the WTC. In addition, these WTC, computed in task (3), are also compared with the WTC present in the Sentinel-3 products, namely through an assessment of both WTC products against Scanning Imaging MWR (SI-MWR), known for their stability and independent calibration.

On the one hand, considering the complexity and large processing time of using a full year of SLSTR SST_{skin} data, and, on the other hand, in order to better account for the SST_{skin} seasonal variability, the three tasks described previously were iteratively conducted on four Sentinel-3A SRAL full 27-day cycles, one for each season of the year.

For the SRAL/MWR sensors, Sentinel-3A Non-Time Critical (NTC) Level 2 ocean data products (1 Hz) from cycles 13, 17, 21 and 24 (winter, spring, summer, and fall of 2017) have been chosen. In the case of the SLSTR sensor, Sentinel-3A NTC Level 2 Water Surface Temperature (WST) data products were used. Data from both sensors were obtained from the Copernicus Online Data Access (CODA) from EUMETSAT (<https://coda.eumetsat.int>). Data from the ECMWF ERA5 atmospheric model were obtained from the Copernicus Climate Change Service (C3S) Climate Data Store (CDS) [12].

2.1. Sentinel-3 SLSTR SST_{skin}

Built on the heritage of the Envisat Advanced Along Track Scanning Radiometer (AATSR) sensor, the SLSTR is a dual-view conical scanning imaging radiometer whose measurements allow the SST_{skin} retrieval on a global scale. The dual-view capability of this instrument enables a better mitigation of atmospheric effects in the SST_{skin} retrieval. The SST_{skin} is obtained from the thermal infrared TB, measured at $3.74 \mu m$ (S7 channel), $10.85 \mu m$ (S8 channel) and $12.00 \mu m$ (S9 channel), and is provided in grid format with a 1 km spatial resolution at nadir (0.009° by 0.009° pixel size) [13].

In a first stage, the SST_{skin} is retrieved from four algorithms, each algorithm considering different channel combinations and viewing geometries. The final SST_{skin} measurement provided for each grid pixel of the SLSTR Level 2 WST data products is chosen based on a hierarchy of preference among the four algorithms retrievals.

The retrieval coefficients for each algorithm are derived using radiative transfer models that simulate the radiances measured by the infrared radiometer [14,15].

2.2. Synergistic Use of the SLSTR and SRAL/MWR Sensors

In the first step of the work, data from each Sentinel-3A SRAL cycle was processed. Only valid ocean observations were selected, with a distance from the nearest coast equal

to or larger than 30 km, to prevent the coastal land contamination in the SRAL and MWR observations, and within the $[-50^\circ, 50^\circ]$ latitude range, the last condition to prevent the ice contamination on the SRAL and MWR measurements occurring at high latitudes.

In the next step, for each SRAL measurement, the corresponding Sentinel-3A SLSTR WST image grid was identified, based on the acquisition time of the SRAL observation and the start-time and end-time of each SLSTR image grid. Since both sensors are operating on the same satellite platform, each SRAL observation is collocated with only one SLSTR image grid. Thus, the synergy process can be easily performed.

To obtain the SST_{skin} measurement from the SLSTR image grid corresponding to each SRAL measurement position, the SLSTR image pixels within a square box centered in the SRAL observation geographical position and with a pre-defined length r were first determined. From this subset of pixels, the mean value of the SLSTR-derived SST_{skin} was computed, using only the pixels with a quality level equal to 5 (best quality SST_{skin}), as advised [16]. In cases where no pixels presented a quality level flag equal to 5, the synergy process could not be carried out and the corresponding SRAL observation was duly annotated.

The length r of the square box was selected based on the acquisition frequency of SRAL observations. Considering 1 Hz measurements, since the along-track satellite velocity is approximately ~ 6.7 km/s, each two consecutive observations will be between 6 km and 7 km apart. Thus, a 6 km-length square box was used, which guarantees that in the synergistic step each SLSTR SST_{skin} grid pixel would be at a maximum along-track distance of ~ 3 km from the SRAL observation.

2.3. Evaluation of the Synergistic Approach against the ECMWF ERA5 Atmospheric Model

Once the synergy process between the SLSTR and SRAL/MWR sensors had been finished, the next step was to compare the SLSTR-derived SST_{skin} with the SST_{skin} from the ECMWF ERA5 atmospheric model.

Based on the geographical coordinates and acquisition time of each SRAL observation, the ERA5 SST_{skin} model grids immediately before and immediately after that time instant were used to perform a spatial and temporal interpolation of the SST_{skin} to the corresponding SRAL observation.

This evaluation was carried out against four SST_{skin} grid versions of the ERA5 model, encompassing two spatial resolutions, 0.25° by 0.25° and 0.50° by 0.50° , respectively, and two temporal resolutions, of 3 h and 6 h, respectively. For each ERA5 model version, the discrepancies between both SST_{skin} sources were evaluated in terms of the mean and standard deviation of their differences, as well as considering the statistical parameters of the linear fit between both sources.

2.4. Assessment of the Impact of Using Each SST_{skin} Source for the Retrieval of the WTC

The last step of this work was the assessment of the impact of using the SST_{skin} derived from the SLSTR sensor and ERA5 model, alongside additional parameters, for the retrieval of the WTC over open ocean. A database of Sentinel-3A SRAL/MWR measurements was built, comprising the measurements from SRAL cycles 13, 17, 21 and 24 for which the SST_{skin} was successfully derived from both sources.

A learning, validation and test datasets was developed from a random split of this global database. The learning dataset, as the name suggests, was used for training the neural network algorithms. The validation dataset was used during the training process, in which the weights and biases of each neuron were adjusted. Its purpose was to evaluate the quality of the training process in the learning dataset of each algorithm and to verify the possible existence of overfitting. Finally, the test dataset's purpose was to assess the performance of each algorithm.

The chosen regression algorithm was the same as the one used in [6–8], i.e., a neural network composed of two layers, one hidden layer with eight neurons and a linear output layer with one neuron. The activation function associated with each neuron of the hid-

den layer was the tan-sigmoid function. The retro-propagation algorithm used was the stochastic gradient descent with momentum (SGDM) algorithm.

Within the scope of this work, four neural network algorithms were developed. All algorithms consider the following three inputs in common: the two MWR brightness temperatures at 23.8 GHz and 36.5 GHz, and the backscatter coefficient σ_0 at Ku band. Each algorithm considers one or two additional parameters, as described below:

- Algorithm 1: SST_{skin} from the ECMWF ERA5 model;
- Algorithm 2: SST_{skin} from the Sentinel-3A SLSTR sensor;
- Algorithm 3: SST_{skin} and the atmospheric temperature lapse rate, γ_{800} , both interpolated from the ECMWF ERA5 model;
- Algorithm 4: SST_{skin} from the Sentinel-3A SLSTR sensor, plus the atmospheric temperature lapse rate, γ_{800} , interpolated from the ECMWF ERA5 model.

The γ_{800} global grids, which describe the linear decrease in atmospheric temperature with altitude, were computed from ECMWF ERA5 atmospheric temperature grids at pressure levels, obtained from the C3S CDS [17]. For each grid pixel, the γ_{800} parameter was computed with a 0.25° by 0.25° spatial resolution and available every 3 h, by performing a linear fit to the atmospheric temperature using the ERA5 pressure levels between 1000 hPa and 800 hPa (pressure levels used, in ascending order of altitude: 1000, 975, 950, 925, 900, 875, 850, 825 and 800 hPa). From the resulting grids, the γ_{800} parameter was spatially and temporally interpolated to each SRAL measurement position.

As output, each neural network algorithm returned the wet path delay (WPD = $-WTC$), in centimetres. The reference WPD values in the train and validation datasets were computed from ECMWF ERA5 global grids of atmospheric temperature and specific humidity at pressure levels, with a 0.25° by 0.25° spatial resolution and available every 3 h, obtained from the C3S CDS [17]. For each grid pixel, the WTC was computed from numerical integration of the two mentioned parameters at thirty-seven pressure levels, from 1000 hPa near the surface to 1 hPa at the top of the atmosphere, using Equation (1):

$$WTC = -(1 + 0.0026 \cos 2\varphi) \int_{P_{sat}}^{P_s} \left(A + \frac{B}{T} \right) q dP \quad (1)$$

where $A = 1.034 \times 10^{-3} \text{ m}\cdot\text{hPa}^{-1}$ and $B = 17.43 \text{ m}\cdot\text{K}\cdot\text{hPa}^{-1}$; q and T are, respectively, the specific humidity, unit-less ($[q] = \text{kg}\cdot\text{kg}^{-1}$), and atmospheric temperature, in K, at pressure P , in hPa, and φ is the latitude of the pixel. The calculated WTC results in meters. Equation (1) provides the highest accuracy of the WTC computation from atmospheric models [3]. More details on the formulation of this equation can be found in [3]. Finally, the WTC was converted to the corresponding WPD values, followed by a spatial and temporal interpolation to each SRAL geographical position.

The independent assessment of each developed algorithm was performed on the test dataset. A comparison was performed with independent WPD sources, namely from SI-MWR, known for their stability and independent calibration. The following SI-MWR were used, available from the NOAA Comprehensive Large Array-data Stewardship System (CLASS) and Remote Sensing Systems (RSS): Advanced Microwave Sounding Unit-A (AMSU-A) on board the NOAA-15, NOAA-18, NOAA-19, MetOp-A and MetOp-B satellites, available at CLASS; Special Sensor Microwave Imager (SSM/I) and SSMIS (SSM/I Sounder) on board F16, F17 and F18 Defence Meteorological Satellite Program (DMSF) satellites, Global Precipitation Measurement (GPM) Microwave Imager (GMI), and AMSR2 on board the Japanese Global Change Observation Mission—Water satellite 1 (GCOM-W1/GCW), available at RSS.

SI-MWR wet tropospheric corrections were computed from the corresponding Total Column Water Vapour (TCWV) products, using the formulation proposed by [18], depicted in Equation (2):

$$WTC = -\left(a_0 + a_1 TCWV + a_2 TCWV^2 + a_3 TCWV^3 \right) TCWV \times 10^{-2} \quad (2)$$

with $a_0 = 6.8544$, $a_1 = -0.4377 \text{ cm}^{-1}$, $a_2 = 0.0714 \text{ cm}^{-2}$, and $a_3 = -0.0038 \text{ cm}^{-3}$. The input TCWV is in centimetres and the resulting WTC in metres. More information about these data is described in [19,20].

For each Sentinel-3A SRAL/MWR measurement of the test dataset, observations from SI-MWR were selected in its vicinity, if available. In order to mitigate the non-collocation effect, both in space and time, between the SI-MWR and the SRAL/MWR, only SI-MWR observations with distances from the SRAL measurements smaller than 50 km and with an absolute time difference smaller than 30 min were selected. Thus, for all the SRAL/MWR measurements on the test dataset for which the collocation with SI-MWR was successful, WPD differences between each algorithm output and the corresponding WPD derived from SI-MWR were calculated. Additionally, the WTC provided in the Sentinel-3A SRAL/MWR products, retrieved from three and five inputs neural networks, were also evaluated against SI-MWR, for purposes of comparison with the developed algorithms in the scope of this study.

3. Results and Discussion

This section presents a description of the results obtained at each step of the work, as well as the corresponding interpretation and discussion.

Regarding the first part of the work, consisting of the synergy between the Sentinel-3A SRAL and MWR sensors with the SLSTR instrument, from the application of a square box with a length of 6 km, it was verified that the percentage of valid SRAL/MWR observations, for which the synergy process with the SLSTR sensor could be successfully applied, was, on average, equal to $29\% \pm 2\%$ only. Thus, in about 70% of the altimeter observations, the synergy process could not be carried out. The available SLSTR SST_{skin} observations are limited to clear sky conditions; thus, the obtained results presented below are also limited to these atmospheric conditions.

Concerning the following step, the results of the SST_{skin} differences between the SLSTR sensor and the ERA5 atmospheric model for Sentinel-3A SRAL cycles 13, 17, 21 and 24, are presented in Tables 1–4, respectively. The N column in Tables 1–4 is related to the number of SRAL/MWR observations for which the SST_{skin} field was successfully derived from the SLSTR sensor products and interpolated from the ERA5 atmospheric model.

Table 1. Statistical parameters of the differences in SST_{skin} derived from the Sentinel-3A SLSTR sensor and the ECMWF ERA5 atmospheric model ($SST_{\text{SLSTR}} - SST_{\text{ERA5}}$), for Sentinel-3A SRAL cycle 13.

ERA5 Resolutions	N	Mean Diff. (K)	Std. Diff. (K)	Scale Factor	Offset (K)
0.25°, 3 h	283,348	0.17	0.42	0.98	4.78
0.25°, 6 h	283,348	0.16	0.42	0.98	4.63
0.50°, 3 h	283,348	0.17	0.43	0.98	4.86
0.50°, 6 h	283,348	0.16	0.43	0.98	4.70

Table 2. Statistical parameters of the differences in SST_{skin} derived from the Sentinel-3A SLSTR sensor and the ECMWF ERA5 atmospheric model ($SST_{\text{SLSTR}} - SST_{\text{ERA5}}$), for Sentinel-3A SRAL cycle 17.

ERA5 Resolutions	N	Mean Diff. (K)	Std. Diff. (K)	Scale Factor	Offset (K)
0.25°, 3 h	259,444	0.18	0.45	0.99	3.65
0.25°, 6 h	259,444	0.18	0.45	0.99	3.48
0.50°, 3 h	259,444	0.18	0.46	0.99	3.85
0.50°, 6 h	259,444	0.18	0.46	0.99	3.67

Table 3. Statistical parameters of the differences in SST_{skin} derived from the Sentinel-3A SLSTR sensor and the ECMWF ERA5 atmospheric model ($SST_{SLSTR} - SST_{ERA5}$), for Sentinel-3A SRAL cycle 21.

ERA5 Resolutions	N	Mean Diff. (K)	Std. Diff. (K)	Scale Factor	Offset (K)
0.25°, 3 h	233,619	0.19	0.44	0.98	4.92
0.25°, 6 h	233,619	0.20	0.44	0.98	5.06
0.50°, 3 h	233,619	0.19	0.45	0.98	5.02
0.50°, 6 h	233,619	0.20	0.45	0.98	5.17

Table 4. Statistical parameters of the differences in SST_{skin} derived from the Sentinel-3A SLSTR sensor and the ECMWF ERA5 atmospheric model ($SST_{SLSTR} - SST_{ERA5}$), for Sentinel-3A SRAL cycle 24.

ERA5 Resolutions	N	Mean Diff. (K)	Std. Diff. (K)	Scale Factor	Offset (K)
0.25°, 3 h	261,579	0.16	0.43	0.98	4.30
0.25°, 6 h	261,579	0.16	0.42	0.98	4.34
0.50°, 3 h	261,579	0.16	0.44	0.98	4.43
0.50°, 6 h	261,579	0.16	0.44	0.98	4.47

As can be observed, there is a good agreement between the SLSTR-derived and ERA5-derived SST_{skin} , among all the used spatial and temporal resolutions of the ERA5 model. This agreement between both sources is consistent with previous studies on the assessment of Sentinel-3 SLSTR SST_{skin} and ERA5 SST_{skin} data [21,22]. Thus, the ERA5 model with a 0.50° by 0.50° spatial resolution and available every 6 h was used henceforth.

The mean and standard deviation maps of the SST_{skin} differences are presented in Figures 1 and 2, respectively, with a 2° by 2° spatial resolution.

From the analysis of Figure 1, representing the mean SST_{skin} differences maps, it can be observed that, globally, the differences between both sources present low values, with a predominant positive mean SST_{skin} difference of ~0.25 K. A persistent variability of the SST_{skin} differences is observed in the location of major oceanic streams, namely the Gulf Stream in the North Atlantic Ocean, Maldives current in the South Atlantic Ocean, the Agulhas stream off the South African coast and the Kuroshio stream along the Japanese coastline, as depicted in the standard deviation maps in Figure 2.

The final database comprised a total of 1 037 990 Sentinel-3A SRAL/MWR measurements with a successful derivation of the SST_{skin} from both sources mentioned previously. The train and validation datasets were composed of 102 131 and 48 210 observations, respectively. The remaining 887 649 observations composed the test dataset.

From the collocation with SI-MWR, using a maximum time difference of 30 min and a maximum distance of 50 km, a total of 61 257 measurements of the test dataset were successfully collocated with the SI-MWR. The results of the Root Mean Square (RMS) of the WPD differences between the operational algorithms and each developed algorithm against SI-MWR are presented in Table 5.

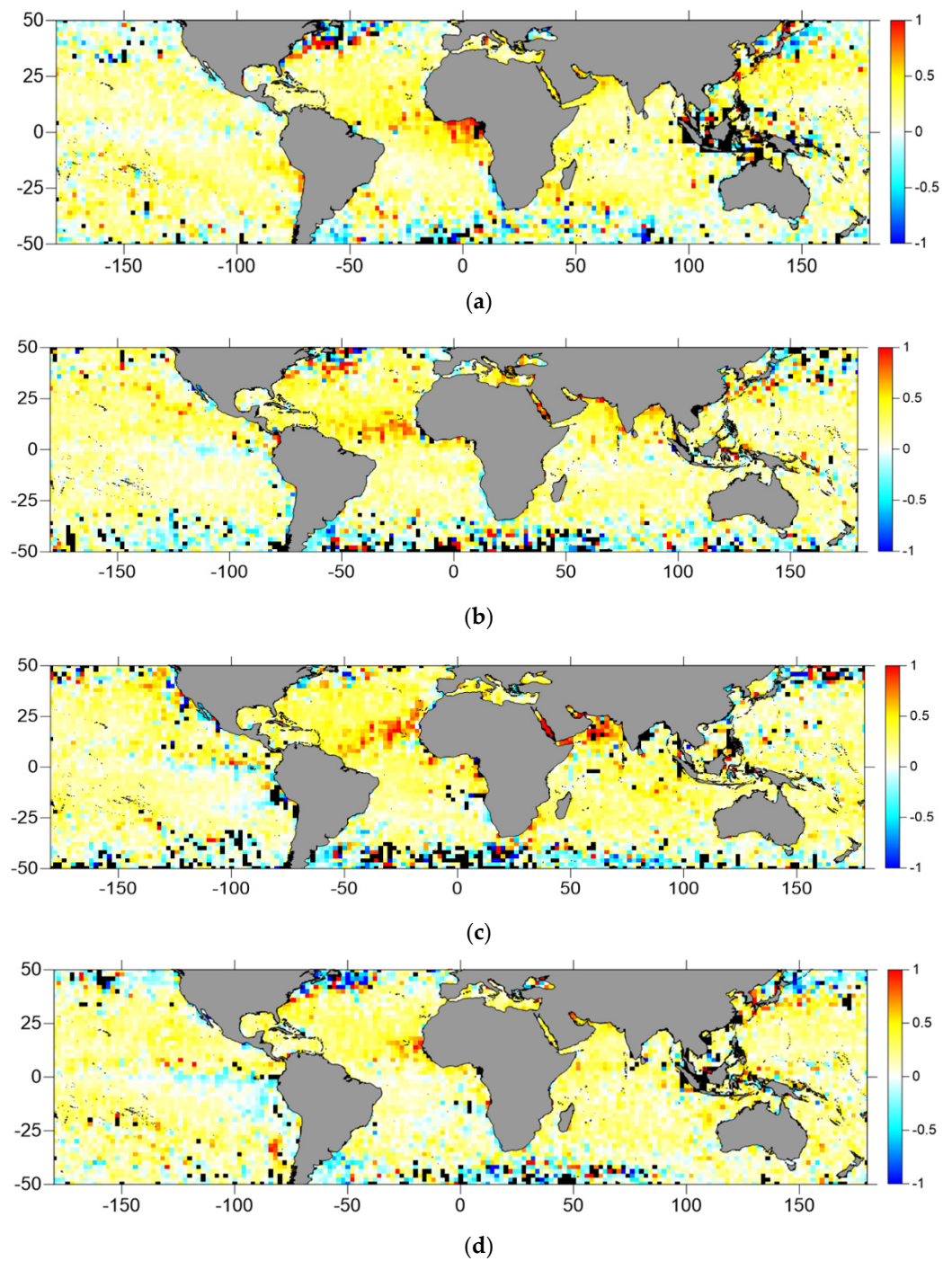


Figure 1. Maps of the mean SST_{skin} differences, in K, between the Sentinel-3A SLSTR sensor and the ERA5 atmospheric model ($SST_{SLSTR} - SST_{ERA5}$), derived for Sentinel-3A SRAL cycles 13, 17, 21 and 24 (subpanels (a–d), respectively), represented with a 2° by 2° spatial resolution. Blank pixels are shown in black.

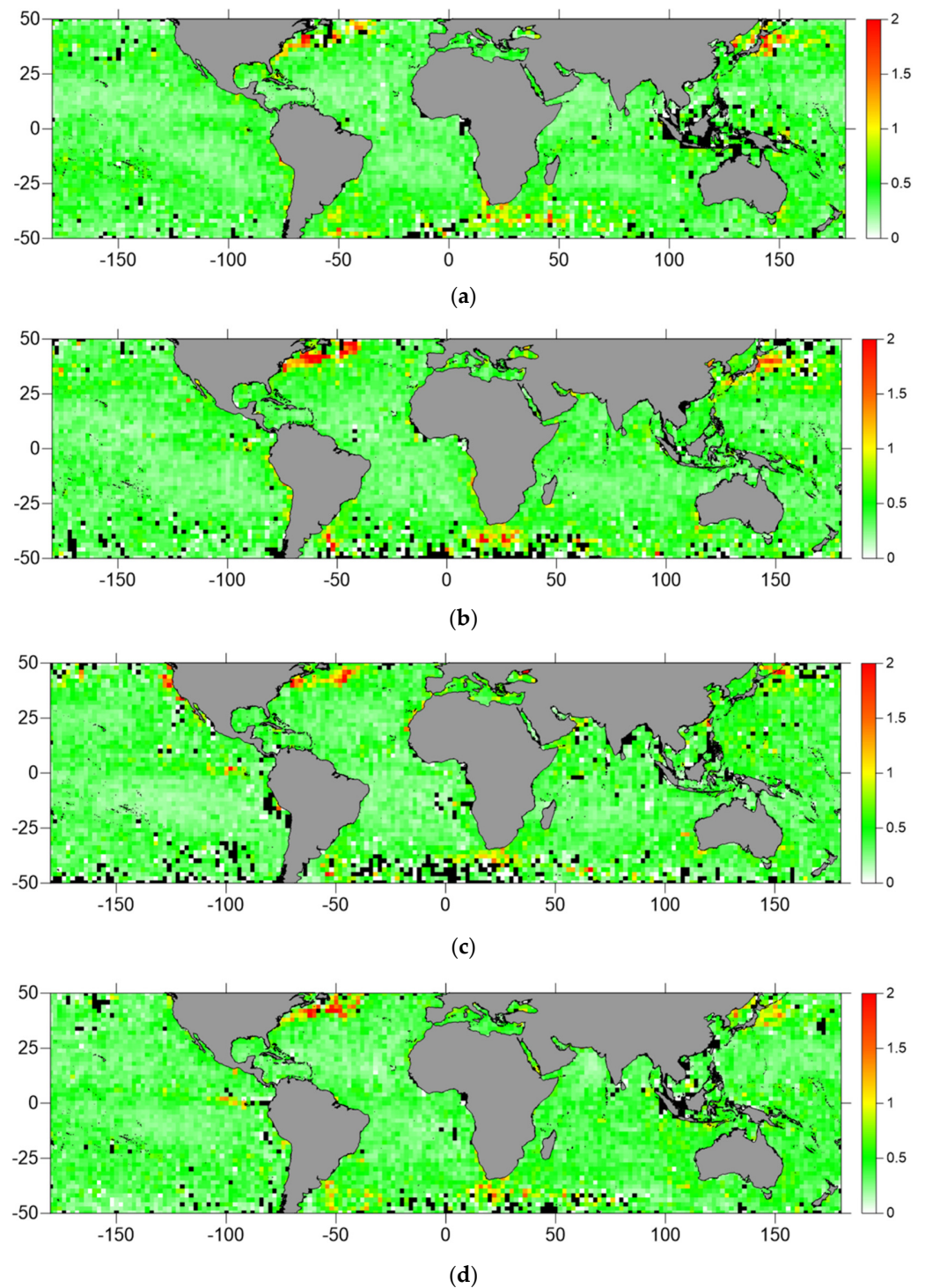


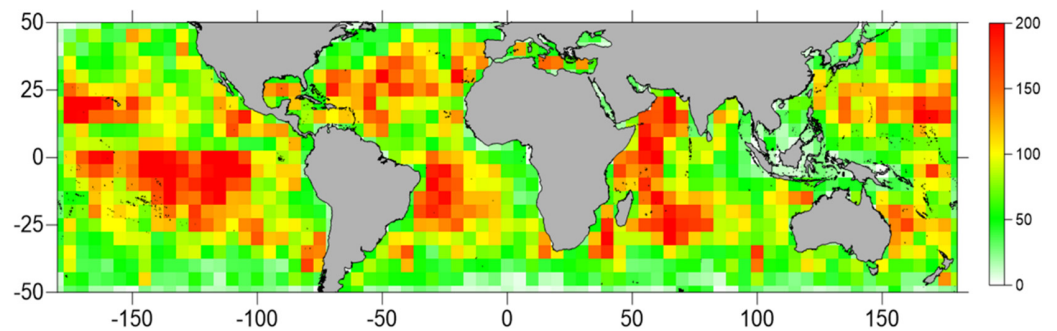
Figure 2. Maps of the standard deviation of SST_{skin} differences, in K, between the Sentinel-3A SLSTR sensor and the ERA5 atmospheric model ($SST_{SLSTR} - SST_{ERA5}$), derived for Sentinel-3A SRAL cycles 13, 17, 21 and 24 (subpanels (a)–(d), respectively), represented with a 2° by 2° spatial resolution. Blank pixels are shown in black.

Table 5. Global RMS of the WPD differences between operational and developed algorithms against SI-MWR.

Algorithm	Inputs	RMS (cm)
Operational 3-Inputs Algorithm	MWR TB _{23.8} , MWR TB _{36.5} , SRAL σ_0 (ku band)	1.12
Operational 5-Inputs Algorithm	MWR TB _{23.8} , MWR TB _{36.5} , SRAL σ_0 (ku band), static SST and static γ_{800}	1.15
1	MWR TB _{23.8} , MWR TB _{36.5} , SRAL σ_0 (ku band) and SST _{ERA5}	1.05
2	MWR TB _{23.8} , MWR TB _{36.5} , SRAL σ_0 (ku band) and SST _{SLSTR}	1.08
3	MWR TB _{23.8} , MWR TB _{36.5} , SRAL σ_0 (ku band), SST _{ERA5} and γ_{800}	1.02
4	MWR TB _{23.8} , MWR TB _{36.5} , SRAL σ_0 (ku band), SST _{SLSTR} and γ_{800}	1.02

Globally, in terms of the RMS of the WPD differences, the results of Algorithm 2 are 0.3 mm worse than those obtained with Algorithm 1, despite being a deterioration on a submillimetre scale. The use of a dynamic γ_{800} (Algorithms 3 and 4, respectively) improved both Algorithms 1 and 2, although the RMS of WPD differences are the same for each SST_{skin} source used. It can also be verified that both operational algorithms are not optimized for the Sentinel-3 mission, given the higher and similar RMS of the WPD differences for both algorithms, when compared to the RMS values of the four developed algorithms. These results agree with those stated by [8,10].

Figure 3 shows the geographical distribution of the collocations of Sentinel-3A SRAL/MWR measurements of the test dataset with SI-MWR. Globally, the number of collocations shows a good representation over open ocean.

**Figure 3.** Number of collocations between Sentinel-3A SRAL/MWR measurements of the test dataset with SI-MWR, represented in a grid with a 5° by 5° spatial resolution.

Concerning the spatial representation of the difference of RMS of WPD differences, Figure 4 shows the difference in RMS values for Algorithm 1 – Algorithm 2. Globally, the results indicate that using the SST_{skin} input from the SLSTR sensor leads to less accurate WPD retrievals, as depicted in Figure 4. However, this degradation in results occurs on a millimetre scale. The majority of the globe is represented by a negative difference in RMS values, which can reach 2.5 mm. The improvement of Algorithm 2 over Algorithm 1 is at its greatest in the Pacific Ocean, in a small region north-east of Australia. In this region, the improvement of Algorithm 2 over Algorithm 1 reaches values up to 0.5 cm and higher.

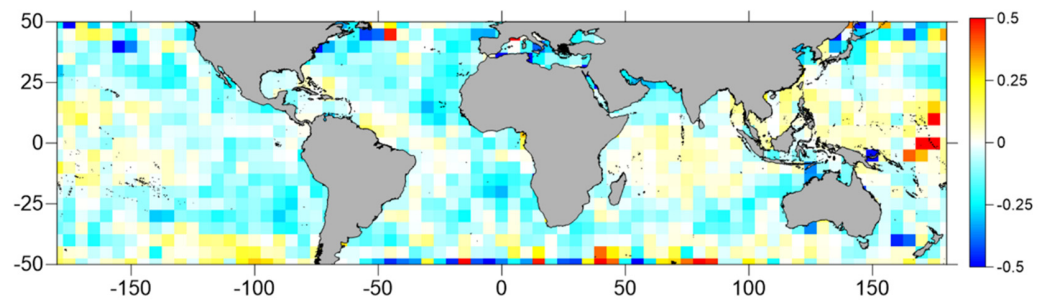


Figure 4. Differences, in cm, between RMS values for Algorithm 1 – Algorithm 2, represented with a 5° by 5° spatial resolution.

In Figure 5, the addition of the γ_{800} input parameter is evaluated. Concerning Algorithm 3, in which the SST_{skin} is derived from the ERA5 model, the addition of γ_{800} does not significantly improve the results (top panel). A larger improvement is noted for Algorithm 4 (bottom panel), specifically outside the $[-25^\circ, 25^\circ]$ latitude window. Within these latitudes, the addition of γ_{800} worsened the results.

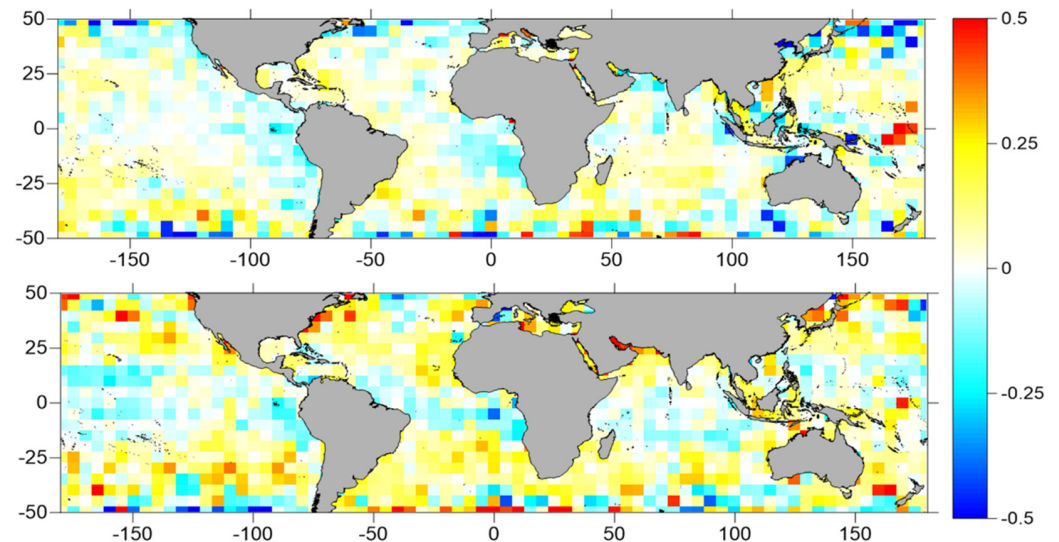


Figure 5. Differences, in cm, between RMS values for Algorithms 1–3 (top panel), and Algorithms 2–4 (bottom panel), represented with a 5° by 5° spatial resolution.

For both Algorithms 3 and 4, an improvement was not observed in regions characterized by a strong atmospheric temperature inversion due to the Hadley cell circulation, namely on the Californian and Peruvian coasts and on the west coast of Africa. These results are consistent with the work presented in [8], although contrary to the results observed in [7]. A possible reason for this has been proposed by [8]—the addition of a dynamic SST already provides information related to the vertical decrease rate in atmospheric temperature with altitude, which makes the addition of the γ_{800} parameter redundant.

In Figure 6, the difference in RMS values for Algorithm 3 – Algorithm 4 is shown. Globally, using the SST_{skin} input derived from the SLSTR sensor, in addition to the γ_{800} parameter, results in less accurate WPD retrievals (at the millimetre scale), sustaining the results already presented above in Figure 4.

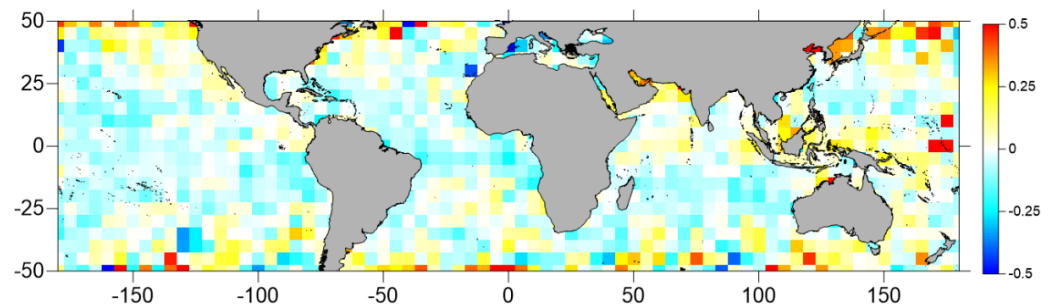


Figure 6. Differences, in cm, between RMS values for Algorithm 3 – Algorithm 4, represented with a 5° by 5° spatial resolution.

In Figure 7, the RMS of WPD differences, function of latitude, for Algorithms 3 and 4 and the operational algorithms are shown. The developed algorithms show an improvement against the operational algorithms in all latitude bands, although the observed improvement is at the millimetre scale. The largest RMS values are observed around the tropics, directly related to a naturally higher concentration of atmospheric water vapour content in this region.

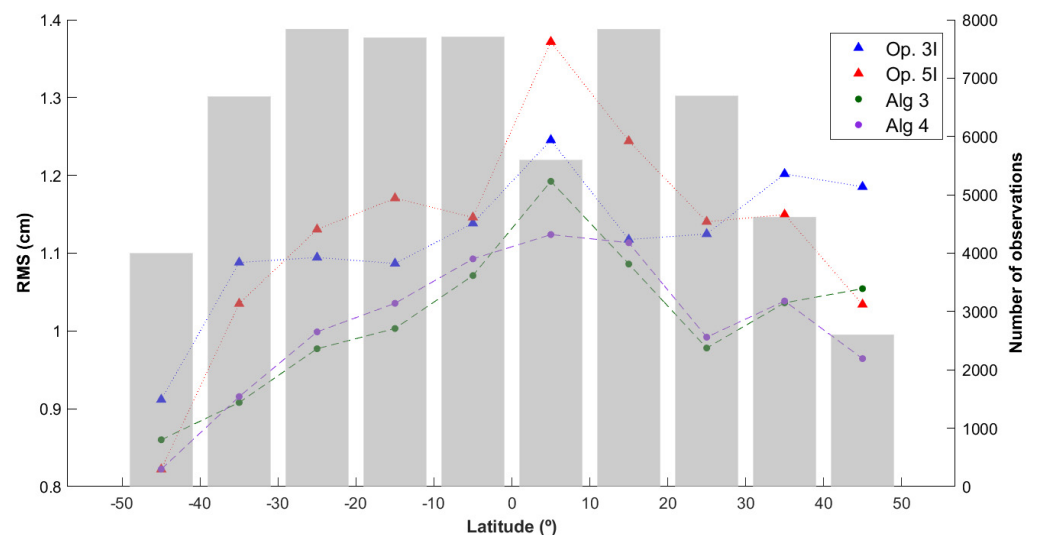


Figure 7. RMS of WPD differences, in cm, for Algorithms 3 and 4 and the operational algorithms, function of latitude, against SI-MWR.

The evaluation of Algorithms 2 and 4 against the operational three-inputs neural network (Op. 3I NN) is shown in Figure 8. The same evaluation against the operational five-inputs neural network (Op. 5I NN) is shown in Figure 9. Globally, both Algorithms 2 and 4 outperform the operational algorithms, namely in the regions of atmospheric temperature inversion mentioned earlier. In addition, the results presented in Figures 8 and 9 sustain the conclusions presented in [8], i.e., the inclusion of a dynamic SST instead of a static one improves the WPD retrievals, while the inclusion of γ_{800} is not significantly impactful.

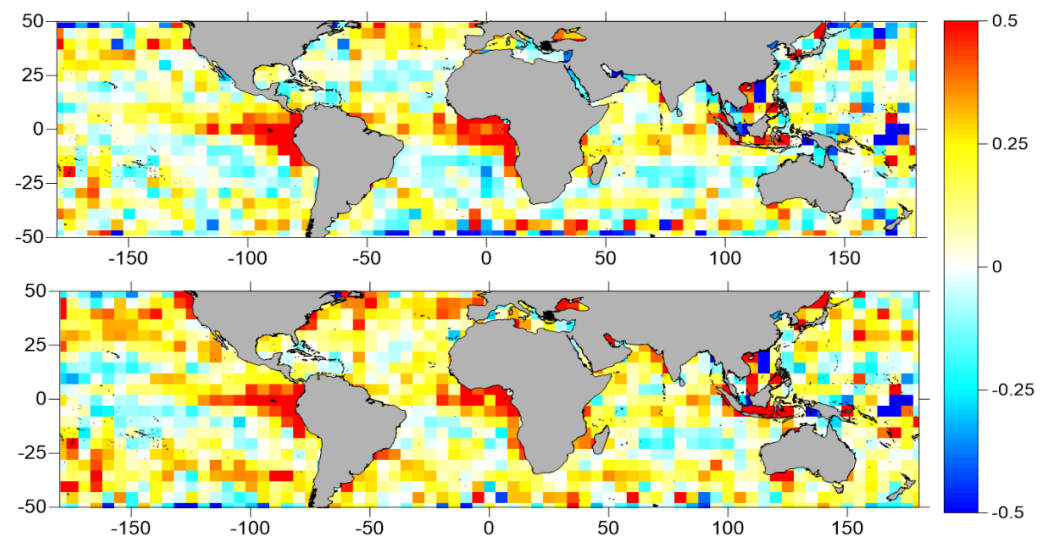


Figure 8. Differences, in cm, between RMS values for Op. 3I NN—Algorithm 2 (**top** panel), and Op. 3I NN—Algorithm 4 (**bottom** panel), represented with a 5° by 5° spatial resolution.

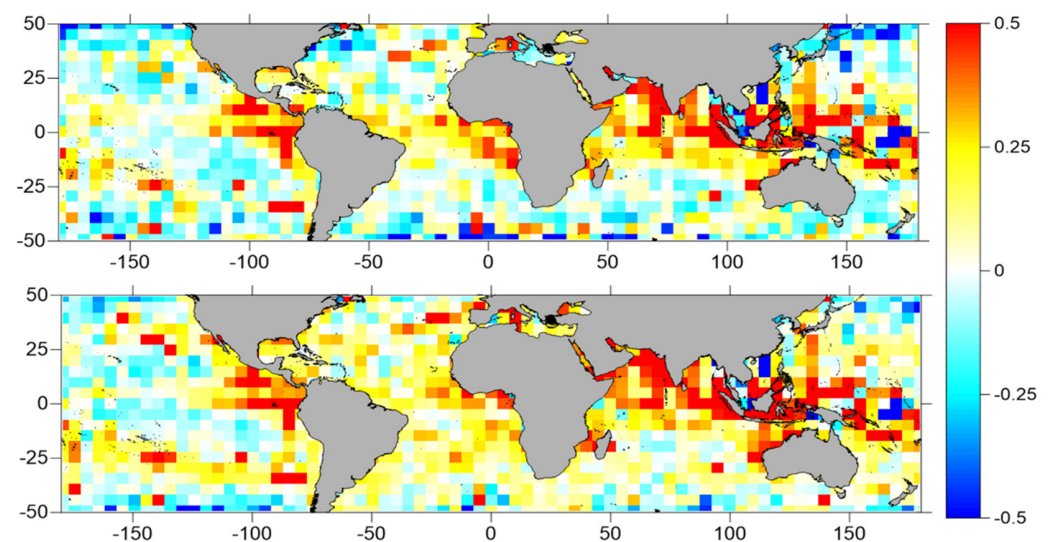


Figure 9. Differences, in cm, between RMS values for Op. 5I NN—Algorithm 2 (**top** panel), and Op. 5I NN—Algorithm 4 (**bottom** panel), represented with a 5° by 5° spatial resolution.

4. Conclusions

This work presents a synergistic approach between the Sentinel-3A SLSTR and SRAL/MWR sensors for the WTC retrieval of SRAL observations. The use of the SST_{skin} geophysical parameter derived from the first sensor, alongside the MWR brightness temperatures, the altimeter backscatter coefficient, σ_0 , and the atmospheric temperature decrease rate, γ_{800} , was analysed. The SLSTR-derived SST_{skin} were compared against the SST_{skin} from the ECMWF ERA5 atmospheric model, and, in a final step, the two SST_{skin} input sources were evaluated in terms of their impact on the WTC retrieval.

The application of the proposed synergistic methodology was limited by the availability of valid SST_{skin} measurements from the SLSTR sensor, which was only successful for 30% of the SRAL/MWR data used. More precisely, the acquisition of SLSTR SST_{skin} observations is limited by the atmospheric conditions at the sensing time, being only available in clear sky conditions. Thus, the obtained results are strictly limited to these atmospheric conditions.

Both SST_{skin} sources show a good agreement, with mean differences for $SST_{SLSTR} - SST_{ERA5}$ in the range [0.16, 0.20] K, with standard deviations ranging between [0.42, 0.46] K.

Globally, the RMS of the WPD differences between the developed algorithms and independent SI-MWR WPD show a 0.3 mm increase when using the SST_{skin} input derived from the SLSTR sensor, instead of the ERA5 model SST_{skin} input. The results show that the addition of the γ_{800} input is not significantly impactful. As proposed by [8], a possible explanation for this may be that the use of a dynamic SST instead of a static one provides information on the atmospheric temperature decrease rate, making the addition of γ_{800} redundant.

All the developed algorithms showed lower RMS of WPD differences with respect to the reference WPD than the operational WTC retrieval algorithms, reaffirming the non-optimization of the latter for the Sentinel-3 mission. Globally, all the developed algorithms 1–4 showed an improvement over the operational algorithms superior to 1 mm, while regionally the enhancement can reach 2.5 mm and higher values.

Based on the obtained results and within the scope of the WTC retrieval over open ocean, this work leads one to conclude that the ECMWF ERA5 atmospheric model is able to accurately capture the spatial and temporal variability of the SST field, being a good SST input source to use for the wet tropospheric correction retrieval. The dependence of the WTC with the SST is lower than with other parameters, such as the MWR brightness temperatures, thus sustaining the non-impactful results when using SLSTR SST_{skin} observations against SST_{skin} values derived from the ERA5 model. Additionally, the use of the ERA5 model presented a lower execution time and lesser computational complexity when compared to the Sentinel-3A SLSTR sensor, making it more appropriate to use on a frequent and operational basis. Furthermore, the SST_{skin} from ERA5 is available for most altimeter points, while that from SLSTR can only be used under clear sky conditions. Even if the use of the SST_{skin} input from the SLSTR sensor improved the WTC computation for altimeter observations, its global use wouldn't be practicable, since the SLSTR-derived SST_{skin} values are only available, on average, for 30% of the altimeter observations for each SRAL cycle.

In view of these results, for the particular application of retrieving the WTC of satellite altimeter observations, there seems to be no added value in having collocated SST and altimeter observations in the future topographic remote sensing missions, such as the Sentinel-3 Next Generation Topography (S3NG-T) Mission.

Author Contributions: P.A. conceived, designed and performed the experiments, and wrote the initial draft of the paper; P.A., T.V., C.L. and M.J.F. analyzed the results, and were involved in the manuscript writing and review. All authors have read and agreed to the published version of the manuscript.

Funding: This research was funded by European Space Agency (ESA), in the scope of the Cryosat project with the reference CRYOSAT- CRYOSAT-2 Ground Segment, IPF/COP Maintenance and Evolution Support, [CCN#5]: Extension of the IPF/COP Maintenance and Evolution Support and upgrades of the Cryosat Ice Processor (Baseline D), C2-CN-ACS-ESL-5353.

Data Availability Statement: Data supporting the reported results can be accessed upon request to the authors.

Acknowledgments: The authors would like to thank Copernicus Online Data Access (CODA) for providing the Sentinel-3A data and the European Centre for Medium-Range Weather Forecasts (ECMWF) and Copernicus Climate Change Service (C3S) for providing the ERA5 atmospheric and surface fields.

Conflicts of Interest: The authors declare no conflict of interest.

References

1. Chelton, D.B.; Ries, J.C.; Haines, B.J.; Fu, L.L.; Callahan, P.S. Satellite altimetry. In *Satellite Altimetry and Earth Sciences: A Handbook of Techniques and Applications*; Fu, L.L., Cazenave, A., Eds.; Academic Press: San Diego, CA, USA, 2001.
2. Cazenave, A. Global sea-level budget 1993–present. *Earth Syst. Sci. Data* **2018**, *10*, 1551–1590.

3. Fernandes, M.J.; Lázaro, C.; Vieira, T. On the role of the troposphere in satellite altimetry. *Remote Sens. Environ.* **2021**, *252*, 112149. [[CrossRef](#)]
4. Keihm, S.J.; Janssen, M.A.; Ruf, C.S. TOPEX/Poseidon microwave radiometer (TMR). III. Wet troposphere range correction algorithm and pre-launch error budget. *IEEE Trans. Geosci. Remote Sens.* **1995**, *33*, 147–161. [[CrossRef](#)]
5. Brown, S. A novel near-land radiometer wet path-delay retrieval algorithm: Application to the Jason-2/OSTM advanced microwave radiometer. *IEEE Trans. Geosci. Remote Sens.* **2010**, *48*, 1986–1992. [[CrossRef](#)]
6. Obligis, E.; Eymard, L.; Tran, N.; Labroue, S.; Femenias, P. First three years of the microwave radiometer aboard envisat: In-flight calibration, processing, and validation of the geophysical products. *J. Atmos. Ocean. Technol.* **2006**, *23*, 802–814. [[CrossRef](#)]
7. Obligis, E.; Rahmani, A.; Eymard, L.; Labroue, S.; Bronner, E. An Improved Retrieval Algorithm for Water Vapor Retrieval: Application to the Envisat Microwave Radiometer. *IEEE Trans. Geosci. Remote Sens.* **2009**, *47*, 3057–3064. [[CrossRef](#)]
8. Vieira, T.; Fernandes, M.J.; Lázaro, C. An enhanced retrieval of the wet tropospheric correction for Sentinel-3 using dynamic inputs from ERA5. *J. Geod.* **2022**, *96*, 1–19. [[CrossRef](#)]
9. Thao, S.; Eymard, L.; Obligis, E.; Picard, B. Comparison of Regression Algorithms for the Retrieval of the Wet Tropospheric Path. *IEEE J. Sel. Top. App. Earth Obs. Remote Sens.* **2015**, *8*, 4302–4314. [[CrossRef](#)]
10. Frery, M.-L.; Siméon, M.; Goldstein, C.; Féménias, P.; Borde, F.; Houpert, A.; Olea Garcia, A. Sentinel-3 Microwave Radiometers: Instrument Description, Calibration and Geophysical Products Performances. *Remote Sens.* **2020**, *12*, 2590. [[CrossRef](#)]
11. Donlon, C.; Berruti, B.; Buongiorno, A.; Ferreira, M.H.; Féménias, P.; Frerick, J.; Goryl, P.; Klein, U.; Laur, H.; Mavrocordatos, C.; et al. The Global Monitoring for Environment and Security (GMES) Sentinel-3 mission. *Remote Sens. Environ.* **2012**, *120*, 37–57. [[CrossRef](#)]
12. Hersbach, H.; Bell, B.; Berrisford, P.; Biavati, G.; Horányi, A.; Muñoz Sabater, J.; Nicolas, J.; Peubey, C.; Radu, R.; Rozum, I.; et al. ERA5 Hourly Data on Single Levels from 1979 to Present. Copernicus Climate Change Service (C3S) Climate Data Store (CDS). Available online: <https://cds.climate.copernicus.eu/cdsapp#!/dataset/reanalysis-era5-single-levels> (accessed on 8 February 2022).
13. Merchant, C. Sea Surface Temperature (SLSTR)—Algorithm Theoretical Basis Document. Available online: https://sentinel.esa.int/documents/247904/349589/SLSTR_Level-2_SST_ATBD.pdf (accessed on 18 February 2022).
14. Merchant, C.; Harris, A.R.; Murray, M.J.; Závody, A.M. Toward the elimination of bias in satellite retrievals of sea surface temperature: 1. Theory, modeling and interalgorithm comparison. *J. Geophys. Res. Oceans* **1999**, *104*, 23565–23578. [[CrossRef](#)]
15. Merchant, C.; Harris, A.R. Toward the elimination of bias in satellite retrievals of sea surface temperature: 2. Comparison with in situ measurements. *J. Geophys. Res. Oceans* **1999**, *104*, 23579–23590. [[CrossRef](#)]
16. EUMETSAT. Sentinel-3 SLSTR Marine User Handbook. Available online: <https://www.eumetsat.int/media/45983> (accessed on 18 February 2022).
17. Hersbach, H.; Bell, B.; Berrisford, P.; Biavati, G.; Horányi, A.; Muñoz Sabater, J.; Nicolas, J.; Peubey, C.; Radu, R.; Rozum, I.; et al. ERA5 Hourly Data on Pressure Levels from 1979 to Present. Copernicus Climate Change Service (C3S) Climate Data Store (CDS). Available online: <https://cds.climate.copernicus.eu/cdsapp#!/dataset/reanalysis-era5-pressure-levels> (accessed on 8 February 2022).
18. Stum, J.; Sicard, P.; Carrère, L.; Lambin, J. Using objective analysis of scanning radiometer measurements to compute the water vapor path delay for altimetry. *IEEE Trans. Geosci. Remote Sens.* **2011**, *49*, 3211–3224. [[CrossRef](#)]
19. Fernandes, M.J.; Lázaro, C. GPD+ Wet tropospheric corrections for CryoSat-2 and GFO altimetry missions. *Remote Sens.* **2016**, *8*, 851. [[CrossRef](#)]
20. Lázaro, C.; Fernandes, M.J.; Vieira, T.; Vieira, E. A coastally improved global dataset of wet tropospheric corrections for satellite altimetry. *Earth Syst. Sci. Data Discuss.* **2020**, *12*, 3205–3228. [[CrossRef](#)]
21. Luo, B.; Minnett, P.J.; Szczodrak, M.; Kilpatrick, K.; Izaguirre, M. Validation of Sentinel-3A SLSTR derived Sea-Surface Skin Temperatures with those of the shipborne M-AERI. *Remote Sens. Environ.* **2020**, *244*, 111826. [[CrossRef](#)]
22. Luo, B.; Minnett, P.J. Evaluation of the ERA5 Sea Surface Skin Temperature with Remotely-Sensed Shipborne Marine-Atmospheric Emitted Radiance Interferometer Data. *Remote Sens.* **2020**, *12*, 1873. [[CrossRef](#)]